

1
2
3
4
5
6
7
8
9
10
11

Extreme Block and Boulder Transport along a Cluffed Coastline during Super Typhoon Haiyan

Andrew B. Kennedy¹, Nobuhito Mori², Tomohiro Yasuda², Takenori Shimozono³, Tori Tomiczek¹, Aaron Donahue¹, Tomoya Shimura², and Yuki Imai²

¹ Department of Civil & Environmental Engineering & Earth Sciences, University of Notre Dame, Notre Dame, IN USA.
² Disaster Prevention Research Institute, Kyoto University, Uji, Kyoto, Japan.
³ Department of Civil Engineering, University of Tokyo, Tokyo, Japan.

12 **Abstract**

13

14 This paper presents data on block and boulder transport during Super Typhoon Haiyan along a
15 4.5km long, low (5-12m) cliffed coastline in Calicoan Island, Eastern Samar, Philippines. Wave
16 runup exceeding 15.2m elevation drove thousands of limestone clasts, many of which – with
17 volumes up to $\sim 83\text{m}^3$ – strongly exceed maximum values stated in the literature to be possible
18 from storms, up to $\sim 280\text{m}$ inland. A few very large clasts ($65\text{-}132\text{m}^3$) were not transported by the
19 waves. As a group, and along with transport reported in May et al. [2015] at a different location
20 during Haiyan, these appear to be the largest blocks verified to have been transported by storm
21 waves, and suggest that a re-evaluation of storm wave transport capability is necessary.
22 Comparison of present results with a global database of storm boulder transport shows a mass-
23 elevation envelope below which transport is observed and above which no transport observations
24 exist.

25 Extension of initiation of motion criteria to include non-rectangular cross-sections significantly
26 reduced inferred velocities necessary for boulder transport during Haiyan, particularly for
27 overturning boulders. Still, the potential range of velocities remained significant once coefficient
28 uncertainty was considered. Lifting/joint-bounded velocity estimates at cliff edges were much
29 larger than for other transport modes, and are difficult to reconcile: it is suggested that processes
30 at cliff edges may be significantly more complex than can be accurately represented with these
31 simple theories.

32

33 **1. Introduction**

34 1.1 Block and Boulder Transport During Large Inundation Events

35

36 Coastal block (secondary axis $b > 4096\text{mm}$) and boulder ($256\text{mm} < b < 4096\text{mm}$) transport has been
37 recorded many times during historical storms and tsunamis [e.g. Goto et al., 2011; Paris et al.,
38 2011; Nandasena et al., 2013; May et al., 2015]. Because large rocks are both durable and easily
39 visible, these clasts are often used as markers to identify the existence and estimate the
40 magnitude of inundation events in the absence of other records (e.g, Imamura et al., 2008). Both

41 existence and magnitude are important for present day planning: evidence from specific sites is
42 valuable for risk evaluation and management, while more general links between hydrodynamics,
43 forces, and transport are useful in predicting conditions that may be experienced at other
44 locations.

45

46 Transport from tropical cyclone waves, which is the focus of this paper, has been reported for
47 one tonne (t) boulders on 20m clifftops in the Okinawan Islands [Goto et al., 2011], and for far
48 larger boulders (for simplicity we omit “block” from most text) at lower altitudes in many other
49 locations [e.g., Khan et al., 2010; May et al., 2015], while strong winter storms have emplaced
50 boulders at high elevations in the Aran Islands, Ireland [Williams and Hall, 2004; Cox et al.,
51 2012], Banneg Island, France [Fichaut and Suanez, 2011], and Enderby Island [McFadgen and
52 Yaldwyn, 1984]. At higher elevations, which will be the focus of this paper, storm wave
53 transport can generate overland features that include ridges (Hall et al., 2008), boulder beaches
54 (Etienne and Paris, 2010), and isolated or scattered boulders (Khan et al., 2010; Goto et al.,
55 2011). Unsurprisingly, locations with larger waves show transport of larger boulders, and to
56 higher elevations. However, although there has been considerable progress made in storm wave
57 transport, it is safe to say that the accurate inference of storm characteristics from boulder
58 deposits is not yet a solved problem.

59

60 Boulder transport has been widely used to infer tsunami inundation in Japan (Hisamitu et
61 al.,2014), Aruba (Scheffers et al., 2005), Iran (Shah-hosseini et al., 2011), Italy (Mastronuzzi et
62 al., 2007) and many other locations. These studies tend to use initiation of motion criteria
63 combined with assumptions about tsunami Froude numbers (Nott, 2003; Nandasena et al., 2011),
64 although numerical models have been used in some instances (Imamura et al., 2008). Direct
65 observations of boulder transport by tsunamis exist for numerous recent historical events [Paris
66 et al., 2009; Bourgeois and MacInnes, 2010; Nandasena et al., 2013] where the magnitude of the
67 tsunami is better known. There is a clear division in size between the largest tsunami boulders
68 [e.g. Frolich et al., 2009; Ramalho et al., 2015] and those emplaced by known storm waves [May
69 et al., 2015], but there is considerable overlap over the observed range.

70

71 While distinction between storm and tsunami transport is straightforward in some instances, it is
72 not always obvious. Parametric force and moment balances [e.g. Nandasena et al., 2011] are
73 often used for both storms and tsunamis to estimate velocities at incipient motion for different
74 transport modes such as overturning, sliding or lifting/saltation. A major assumption is usually
75 then made where storm waves have a local Froude number of unity, while tsunamis have Froude
76 numbers of two. This leads directly to the assumption that storm waves must be four times larger
77 than tsunamis to transport the same size boulders (Nott, 2003). This large discrepancy often leads
78 to inferred storm wave heights that are unrealistically large while tsunami heights are much
79 smaller and more reasonable (e.g. Kelletat et al., 2004). However, although widely used,
80 incipient motion relations and the assumptions they are based on have received very little
81 validation; i.e. velocity and height inferences have not been independently confirmed. Thus,
82 there remains an active debate over the origins of some boulder fields and the methods used to
83 estimate event magnitudes – these disputes may be partially resolved from analysis and
84 intercomparison of transport during both storm and tsunami mega-events. In this paper we
85 present observations of block and boulder transport during Typhoon Haiyan. Results are used to
86 help define the envelope of transport space during extreme storms, and to evaluate and improve
87 widely-used techniques for inferring event fluid velocities.

88

89 1.2 Super Typhoon Haiyan

90 With estimated one minute sustained winds of 170 knots (87m/s), Super Typhoon Haiyan may
91 have been the strongest landfalling tropical cyclone of the satellite era when it passed the
92 Philippine islands of Samar and Leyte on November 7, 2013 (Fig. 1a) [Joint Typhoon Warning
93 Center, 2013]. Areas near landfall suffered catastrophic damage, with more than 6,000 fatalities
94 and greater than one million buildings damaged or destroyed. [National Disaster Risk Reduction
95 and Management Council, 2014]. Largest storm surge values were found in shallow San Pedro
96 Bay near the city of Tacloban, with surge to 5-6m, and runup to 7-8m [Tajima et al., 2014, Mas
97 et al., 2015]. In contrast, the open Pacific coast near the present study region had predicted
98 offshore surge of less than 0.3m because bathymetry drops steeply into the Philippine Trench
99 [Mori et al., 2014]. However, Figure 1a shows extreme waves during Haiyan, with a hindcast
100 peak significant wave height of $H_s=18.7\text{m}$ just offshore of the study region [Mori et al., 2014].

101 The site itself, as shown in Figures 1b and 2a, is a region of low limestone cliffs (5-12m cliff
102 elevations from mean sea level, MSL) north of Ngolos Beach on Calicoan Island. The cliffs are
103 from the Upper Pliocene-Pleistocene Calicoan Limestone formation, which extends north from
104 Calicoan Island with outcrops along the eastern coast of Samar. The rock is a “reef facies
105 limestone built as distinct reefs along the coast by mollusks and algae”, with “corals, shells, and
106 algae structures” very evident (Travaglia et al., 1978). Study region bedrock topography seen in
107 Figure 2b shows heavy karst weathering with typical vertical roughness of 0.5-1m, and with
108 extremely sharp phytokarst pinnacles in the sea-spray region (Taborosi and Kazmer, 2013).
109 Large caves and other karst features are found nearby. Some sections of coastal cliffs are fronted
110 by horizontal shore platforms with around 1-2m elevation MSL and width ~20m, while other
111 sections have vertical or overhanging cliffs with no platforms. In non-storm conditions, waves
112 impacting on these cliffs generate vertical jets extending well over 10m into the air (Supporting
113 Video S1). During Haiyan, runup overtopped all coastal cliffs in the study region. While beaches
114 north and south of these cliffs are fronted by fringing reefs several hundred meters wide as seen
115 in Fig. 1b, no reefs are found in front of the cliffs (Fig. 2a). Away from the immediate cliff faces,
116 elevations increase gradually to much larger hills and cliffs 100-400 meters inland. Figure 1c
117 shows some partial transects taken through the boulder transport region.

118

119 Runup was extreme during Haiyan, with nearby magnitudes measured up to 14.1m above sea
120 level [Tajima et al., 2014; Shimozono et al., 2015; Roeber and Bricker, 2015]. Satellite-visible
121 vegetation loss and soil erosion were observed for several hundred meters inland, often with
122 prominent terminal debris clusters often composed of logs, sometimes interspersed with
123 limestone boulders. The extreme runup dislodged and transported inland large numbers of these
124 boulders, many of which were large enough to be clearly visible on satellite photographs.

125

126 **2. Inundation and Boulder Transport on Calicoan Island Cliffs**

127 Boulders in the 4.5km study region (Fig. 1b, 2a) on Calicoan Island were studied during eight
128 days of ground-level and aerial reconnaissance in January and November, 2015; and using pre-
129 and post-storm satellite images. Large boulder transport during Haiyan has previously been
130 reported by May et al. [2015] onshore of a wide fringing reef approximately 40km north of the

131 present site. Boulder masses were estimated at up to 180t at sea level, with smaller boulders
132 transported at higher elevation. Kennedy et al. [2016] examined and modeled runup and smaller
133 boulder transport immediately south of the present study region over a smoother beach
134 topography, and found a strongly nonlinear dependence of transport elevations and inland
135 distances on incident wave height. The present study largely differs from these two previous
136 works in that it focuses on transport in a higher elevation cliff region without fringing reefs. Sea
137 level boulders in pocket beaches along the cliffed coastline, some of which were quite large (Fig.
138 3), were neglected in this survey in favor of higher elevation transport.

139

140 As shown in Fig. 4, the study site contains many Haiyan-transported boulders and blocks with
141 characteristic lengths $>1\text{m}$, with totals likely in the low thousands. Exact numbers could not be
142 determined both because of the large number of clasts and because of vegetation regrowth which
143 often required trail-cutting to find and reach individual boulders. Figure 6 gives examples of
144 some of the boulders observed here, while Table 1 presents data on the largest boulders
145 measured here directly. Supplemental Figures S.1.1-S.1.15 give aerial and ground level
146 snapshots for boulders in Table 1. Most large boulders were very angular to subangular, often
147 with different faces showing highly different weathering and angularity (Fig. 7). Although most
148 faces showed high angularity arising from recent breakage and erosional karst weathering, lower
149 faces (pre-storm) on boulders that had already been detached from bedrock tended to be much
150 more rounded. Although all clasts were limestone, colors varied significantly and gave
151 indications of processes and locations. Dark gray upper faces indicated an exposure to both
152 direct sea spray and sunlight, while lighter gray showed a more inland origin. White faces
153 indicated rock that was not directly exposed to the sun. Transported boulders typically had
154 moderate to low sphericity. In many ways, these properties are typical for coastal karst
155 landscapes in humid tropical regions (Taborisi and Kazmer, 2013).

156

157 All observed clasts of boulder size or greater appeared to originate subaerially from either the
158 cliff edge or the bedrock somewhat inland. Some boulders had clearly been generated in earlier
159 inundation events and were moved further landward by Haiyan, while others were freshly
160 detached from the bedrock. Karst processes including flowstone and small solution columns

161 showed some existing boulders' pre-storm locations on bedrock (Fig. 8). Fresh scars showed
162 other locations where new boulders had been generated (Fig 9). However, except in a few cases
163 (boulders 999, N0, N2), it proved impossible to match final and initial locations conclusively.
164 Validating motion during Haiyan was made difficult by the complete vegetative cover pre-storm,
165 rendering it impossible to see boulder locations on satellite images. However, in many cases the
166 presence of perishable debris such as plant material underneath boulders gave conclusive proof
167 of transport, as did signs of overturning/rolling, including new orientations of originally
168 downward facing sides, and impact scars. The color and weathering of bedrock underneath a
169 boulder gave additional evidence of motion in some cases.

170

171 Cobble-sized clasts were commonly observed: a small fraction (probably less than 1%) were
172 rounded to well-rounded, suggesting a subaqueous origin (Fig. 10), but no detailed statistics were
173 taken. Almost no sand was observed on this rocky landscape, likely from a lack of source
174 material and in direct contrast to the sandy inland deposits observed immediately to the south
175 [Kennedy et al., 2016]. Inland runup limits shown in Figure 4 were estimated using trimlines and
176 debris lines visible on both standard Google Earth imagery and commercially available 0.5m true
177 color satellite images of the study area, with oblique aerial images used to verify features. These
178 same tools were used to identify locations and approximate sizes of some of the larger boulders,
179 but could not provide a complete picture. More accurate ground-level reconnaissance thus
180 concentrated on some of the largest boulders observed in satellite images and the regions around
181 them.

182

183 Boulder principal axis lengths (a,b,c), locations, and elevations above mean sea level were
184 measured directly from ground-level observations using measuring tapes and kinematic GPS
185 (n=76), or (a,b) and locations were estimated from satellite observations (n=379). The satellite
186 observations could reliably detect only larger boulders that differed in color from the
187 surrounding bedrock, and were not covered in debris or hidden by vegetation. Based on ground
188 level observations, satellites provided a severe undercount of boulder quantities, and numbers of
189 intermediate-sized boulders ($a < 2.5\text{m}$) are many times greater than suggested by satellite
190 observations. Larger boulders were also undercounted, but by a lesser margin. Direct ground

191 measurements given in Table 1 for the largest boulders show 8 storm-transported boulders with
192 $a > 7\text{m}$ (maximum $a = 7.7\text{m}$) and 10 boulders with masses exceeding 100t (maximum 208t). Figure
193 4 shows locations and axis lengths both for directly measured boulders, and for those with sizes
194 estimated from satellite observations (though these are without confirmation of transport during
195 Haiyan). Hundreds of boulders were observed by satellite throughout the study area at up to
196 280m from the shoreline, with on-ground confirmation to estimated inland runup limits.
197 Spatially, boulders did not form the large ridges found on some locations in Ireland or the
198 Caribbean [Williams and Hall, 2004; Watt et al., 2010] which are a signature of storm deposits
199 [Paris et al., 2011], although clustering is evident. As seen in Fig. 11, observed debris clusters
200 were often composed of floating vegetation with boulders sometimes interspersed, while others
201 were primarily rocky. The lack of coherent ridges suggests that inundation events with
202 magnitudes comparable to Haiyan are relatively rare; alternatively, existing ridges may have
203 been destroyed during Haiyan. Beaches composed of smaller boulders and cobbles were found
204 well inland in numerous locations (Fig. 10), suggesting that these were in the swash zone during
205 Haiyan.

206

207 Elevations from MSL were measured at the highest point of many transported boulders, as it was
208 assumed that minimum inundation heights reached at least to this level. Results presented in
209 Table 1 are remarkably consistent, with 14 boulders showing minimum inundation levels of 14m
210 above MSL, and a maximum measured boulder top elevation of 15.2m very near to a vegetative
211 debris cluster with almost identical height. Other measured debris elevations tended to be lower,
212 as vegetative debris would need to be very tall to reach boulder crests. Measured inundation here
213 exceeds the maximum value of 14.1m during Haiyan given in Shimozono et al. [2015] taken less
214 than 20km from the study site. As boulder transport likely requires inundation significantly
215 deeper than the boulder top surface, it is probable that runup elevations exceeded even the 15.2m
216 shown here, but this cannot be proved.

217

218 Of large boulders visible on satellites and subsequently visited during ground level observations,
219 only two showed no evidence of motion (Fig. 12). These were seen on satellites and in aerial
220 imagery to have grey (phytokarst) upper faces, indicating that they had not rolled, and their

221 motion was considered uncertain prior to ground-level reconnaissance. Both were very large
222 with (a,b,c)= (7.5,6.5,4.5)m, (8.0,5.0,2.7)m (Table 1), and may be formed-in-place tower karst
223 features [Myloie, 2007; Ford and Williams, 2007] rather than boulders moved by storms or
224 tsunamis. However, this is not certain and it is quite possible that they were generated by an
225 inundation event more powerful than Haiyan. Two other smaller boulders measured during
226 ground reconnaissance were believed to not have moved, with both showing pre-storm root
227 systems and partial burial.

228

229 Boulders here seen in satellite photos up to the estimated runup limit have been visually
230 confirmed in some (but not all) cases. Since the visible runup limit extends to almost 300m
231 inland in some portions of the present study, inland distances of boulder transport and runup are
232 much further than is possible from a single wave. In this case, infragravity runup as
233 demonstrated by Shimosono et al. (2015), Roeber and Bricker (2015), and Kennedy et al. (2016)
234 appears to be the likely mechanism. The present low cliff topographies are significantly different
235 from these other locations where infragravity runup has been noted, but still water storm surge
236 was much too low to account for inundation (Mori et al., 2014) and transport and other
237 explanations do not appear to satisfy the observed features. However, until experiments or
238 computations are performed on low cliff topographies such as are found here, details are to some
239 degree speculative.

240

241 Frequently, the ability of storm waves to transport large boulders has been discounted when
242 compared to tsunamis. Numerous publications [Benner et al., 2010; Scheffers and Kinis, 2014;
243 Erdmann et al., 2015] have suggested that boulders with volumes greater than $\sim 20\text{m}^3$ (sometimes
244 reported as 20 tonnes) could not be significantly transported by storm waves. These volumes are
245 greatly exceeded by present results. Using conservative (low) estimates of volume as
246 $V = 0.6abc$ [Engel and May, 2012; May et al., 2015], ground-level observations yield 22
247 boulders with volumes greater than 20m^3 and two large boulders with estimated volumes of
248 83m^3 each. (May et al., 2015 also report volumes up to 75m^3 .) Thus, it appears that the envelope
249 of block sizes transportable by storm waves can be extended to at least 80m^3 : because a

250 relatively small portion of the post-Haiyan coastline has been surveyed for boulder transport, this
251 limit cannot be stated as definitive.

252

253 Maximum boulder quantities here ($a=7.7\text{m}$, $\text{mass}\sim 208\text{t}$, $\text{runup}>15\text{m}$) are highly comparable to
254 boulders reported to have been transported by the 2011 Tohoku earthquake tsunami ($a=6.5\text{m}$,
255 $\text{mass}\sim 140\text{t}$, $\sim 18\text{m}$ local runup) [Nandasena et al., 2013]; in the 2006 Kuril Islands tsunami
256 ($a=3\text{m}$, $\text{mass}\sim 37.5\text{t}$, $\sim 15\text{m}$ runup) [Bourgeois and MacInnes, 2010], and in Sumatra during the
257 2004 Indian Ocean tsunami ($a=7.2\text{m}$, $\text{mass}\sim 85\text{t}$, $\sim 20\text{m}$ local runup) [Paris et al., 2009]. However,
258 maximum boulder dimensions here are less than those inferred from megatsunamis in Ishigaki
259 Island, Japan ($a=12.4\text{m}$, $\text{mass}>500\text{t}$, runup $\sim 30\text{m}$) [Imamura et al, 2008; Hisamatsu et al., 2014],
260 Tonga ($a=15\text{m}$, $\text{mass}\sim 1600\text{t}$, runup $>20\text{m}$) [Frohlich et al., 2009]; and Santiago Island, Cape
261 Verde ($\text{mass}\sim 700\text{t}$, runup $\sim 220\text{m}$) [Ramalho et al., 2015].

262

263 **3. Present Observations in Global Context**

264 To provide a broader picture of storm boulder transport, masses and elevations from the present
265 study were combined with other literature values as shown in Figure 13, with details in
266 Supplementary Material. Here, we only plot locations with reported storm transport, and a few
267 locations with uncertain transport: sites with inferred or observed tsunami transport are not
268 included. A clear envelope can be seen, with boulder transport possible below certain elevations
269 at a given mass, and no transport observed above. Unsurprisingly, maximum boulder masses
270 decrease strongly with increasing elevations. The upper limits of the envelope are dominated by
271 very large waves from winter storms [McFadgen and Yaldwyn, 1984; Williams and Hall, 2004;
272 Hansom et al., 2008; Etienne and Paris, 2010; Fichaut and Suanez, 2011], and from regions with
273 strong tropical cyclones [Goto et al., 2011; Khan et al., 2010; May et al., 2015; present study].
274 All of these regions have extreme waves, with maximum potential significant wave heights
275 likely to be in the range $H_s=15\text{-}20\text{m}$.

276

277 To demonstrate the usefulness of a such an envelope, three locations with some uncertainties in
278 boulder transport were plotted along with the known storm transport: Jones et al. [1992] from

279 Grand Cayman Island, Nakamura et al. [2014] from Lanyu Island, Taiwan, and Hearty [1997]
280 from Eleuthera Island, Bahamas. All three locations are subject to extreme tropical cyclones but
281 transport has not been definitively distinguished between tsunamis and storms. The megaclasts
282 of Hearty [1997] have the additional complication of being reported to be formed-in-place
283 features and not wave-transported at all [Myroie, 2007], although this is strongly disputed
284 [Hansen et al., 2016]. Both the Taiwan and Cayman data fall very easily within the range of
285 observed storm transport, which does not guarantee that boulders were transported by storms, but
286 adds additional evidence to support the possibility of storm transport. The Eleuthera data plots
287 quite differently. Here, boulders (with sea levels corrected to the geological period from which
288 they are said to have been generated) have, with a few exceptions, masses much larger than
289 anything observed to have been transported by storm waves. If these were storm transport, either
290 site conditions were absolutely ideal to allow such large clasts to be transported, or storm waves
291 were much larger than modern observations. The larger waves hypothesis has been put forth by
292 Hansen et al. [2016], who argued that climatic conditions caused storms in the late-Eemian to
293 have waves larger than are found even in the strongest tropical cyclones today; however, none of
294 this can yet be considered definitive.

295

296 This analysis is not complete. Local setting and inland distance, the presence or absence of reefs,
297 boulder shape, and many other properties will have significant influence on whether transport
298 occurs. However, the most obvious omission here is that all boulder data are plotted together
299 even though wave forcing differs between sites. Thus, the envelope arises entirely from sites
300 with the strongest wave forcing: for sites with weaker wave forcing, it is not clear what form the
301 envelope would take. A more general analysis would nondimensionalize all data by wave
302 heights, boulder shape, rock density and other factors to give results that could be compared
303 across the wave height and boulder size range. This would allow observed boulder transport for
304 large boulders in high waves to be scaled to predict small boulder transport in small waves, and
305 vice-versa. However, this type of analysis would require measured or hindcast wave heights
306 either for specific storms known to cause transport, or for storm climatology at a given site. Such
307 a hindcast is an extremely computationally-intensive undertaking, but is just now of the cusp of
308 what is possible. The authors are in beginning stages of such hindcasts and will report on them as
309 results become available.

310

311 **4. Initiation of Motion for Observed Boulders**

312 Initiation of motion criteria for boulder transport have historically been the primary methodology
313 to infer hydrodynamics for inundation events in which other data do not exist. These
314 methodologies apply drag, lift, gravitational, frictional, and sometimes inertial force or moment
315 balances to determine minimum fluid velocities for boulders to slide, overturn, or lift from
316 previously stationary positions. Many assumptions have been made to arrive at these relations:
317 that boulders are shaped like rectangular prisms, that force coefficients are known to a sufficient
318 degree of accuracy, and that initiation of motion leads to permanent motion and not just rocking
319 in place (Weiss and Diplas, 2015). Of course, none of these assumptions are entirely true: still,
320 some effects of these uncertainties may be investigated by varying parameters over plausible
321 ranges, and by extending relations to include the effects of non-rectangular boulders. Once
322 known, this degree of uncertainty in hydrodynamics feeds directly into incident wave or tsunami
323 forcing, giving a better understanding of possible conditions leading to transport. Typhoon
324 Haiyan provides a good opportunity to test relations, to see the range of conditions that may be
325 possible, and to evaluate the plausibility of results.

326

327 3.1 Initiation of Motion for Non-Rectangular Boulders

328

329 The approach taken here follows closely the work of Nandasena et al. (2011), but without *a*
330 *priori* assumptions of shape. For a non-rectangular-prismatic boulder with principal axis lengths
331 (a, b, c) , the volume will be $V = C_v abc$, where C_v is a dimensionless factor between 0 and 1.
332 Likewise, the frontal area visible to flow perpendicular to long axis a will be $A_f = C_f ac$ and
333 plan area for lift will be $A_p = C_p ab$, where both C_f and C_p are dimensionless factors between
334 zero and 1. All factors $[C_v, C_f, C_p] = 1$ for a rectangular prism, but other values can be applied
335 to any boulder shape as appropriate. The submerged weight is then $W = C_v (\rho_s - \rho_w) g abc$ where
336 ρ_s is the rock density, ρ_w is the fluid density, and g is gravitational acceleration. On a slope of
337 angle θ (positive uphill), the slope-perpendicular weight will be $F_{gz} = W \cos \theta$ and the

338 downslope component will be $F_{gx} = W \sin \theta$. When acted on by a fluid with velocity U parallel
339 to the ground, the drag force will be $F_d = 0.5\rho_w C_d C_f a c U^2$, where C_d is the drag coefficient, and
340 the lift force will be $F_l = 0.5\rho_w C_l C_p a b U^2$. Inertial forces are $F_I = C_m C_v \rho_w a b c \frac{DU}{Dt}$, where C_m is
341 the inertial coefficient. The frictional resistance to motion will be $F_f = \mu_s (F_{gz} - F_l)$, where μ_s is
342 the coefficient of static friction. For incipient sliding motion, the force balance is then
343 $F_d + F_l = F_f + F_{gx}$, which leads directly to:

$$344 \quad U_{slide}^2 \geq \frac{2C_v c \left[(\rho_s / \rho_w - 1) g (\mu_s \cos \theta + \sin \theta) - C_m \frac{DU}{Dt} \right]}{C_d C_f c / b + \mu_s C_l C_p} \quad (1)$$

345
346 For overturning motion, moments are summed about the boulder toe. For a boulder that is a
347 rectangular prism, the gravitational restoring moment arm will be $b/2$. However, for a non-
348 rectangular boulder (with corners and edges rounded or cut off), we take the pivot point as εb
349 from the corner, which gives a slope-perpendicular restoring moment arm of $l_{gz} = b(1/2 - \varepsilon)$.
350 The downslope component of weight will have a moment arm of l_{gx} : here we take this to remain
351 unchanged from its rectangular value at $l_{gx} = c/2$, but it could differ with shape. Drag and
352 inertial forces will have moment arms of l_d and l_I : here we both take as of $[l_d, l_I] = c/2$, while
353 lift force will have a moment arm of l_l which we take here as $l_l = b(1/2 - \varepsilon)$. Frictional forces
354 have a moment arm of zero. The moment balance about the toe for incipient overturning is then:
355 $F_d l_d + F_l l_l + F_I l_I = F_{gx} l_{gx} + F_{gz} l_{gz}$. Simplification of this for assumed moment arms here yields:

$$356 \quad U_{roll}^2 \geq \frac{2C_v c \left[(\rho_s / \rho_w - 1) g \left(\cos \theta (1 - 2\varepsilon) + \sin \theta \frac{c}{b} \right) - C_m \frac{c}{b} \frac{DU}{Dt} \right]}{C_d C_f c^2 / b^2 + C_l C_p (1 - 2\varepsilon)} \quad (2)$$

357
358 For incipient lifting, the force balance is $F_{gz} = F_l$, which gives directly the relation used for joint-
359 bounded computations:

360
$$U_{lift}^2 \geq \frac{2C_v(\rho_s / \rho_w - 1)gc \cos \theta}{C_l C_p} \quad (3)$$

361

362 The question now becomes how to define the unknown shape coefficients C_v , C_f , C_p , and ε ,

363 and moment arms. The best way to do this would be to measure detailed boulder shapes directly

364 at field sites (e.g. Gienko et al., 2014; May et al., 2015); however, this was not accomplished

365 here because of time and logistical concerns. Instead, we make simple analytical changes to the

366 rectangular prism and cut off all edges and corners at distances $\varepsilon(a, b, c)$ as shown in Figure 14.

367 This gives coefficients of $(C_v, C_f, C_p) = \left(1 - 6\varepsilon^2 + \frac{16}{3}\varepsilon^3, 1 - 2\varepsilon^2, 1 - 2\varepsilon^2\right)$, governed by the single

368 dimensionless parameter ε which also yields the overturning moment arm reduction in (2). If

369 hydrodynamic parameters C_d and C_l are known, along with frictional coefficient μ_s , bed angle

370 θ , and rock density ρ_s , minimum velocities to initiate different modes of motion may be

371 computed. As the fraction of edges cut off, ε , approaches zero, equations (1-3) revert to the

372 Nandasena et al. (2011) relations.

373

374 3.2 Inertial Forces and Scaling in Runup Bores

375 Inertial forces have proved problematic for incipient motion studies. Clearly, inertial forces

376 (driven by accelerations) and drag forces (driven by velocities) will not be maximum at the same

377 time. Additionally, acceleration in bore fronts may be maximum when the boulder is not fully

378 immersed, making it difficult to apply standard coefficients. Finally, well-known inertial

379 coefficients for free-stream flow are not the same as those for the wall-bounded flow found here

380 (Dean and Dalrymple, 1991). Thus, the inclusion of inertial forces involves approximation and

381 uncertainty. Still, if these uncertainties are quantified and evaluated, we may still obtain useful

382 information.

383

384 For submerged boulders, inertial forces are usually ignored as unimportant in initiation of motion

385 criteria (Nott, 2003; Nandasena et al.; 2011). For subaerial boulders, inertial forces are

386 sometimes included but given a small value (Nott, 2003), or omitted entirely (Nandasena et al.,
 387 2011). However, this is difficult to justify in a runup bore, where accelerations are certainly
 388 large: Jensen et al. (2003) showed accelerations exceeding 0.5g on a steep laboratory beach over
 389 much of the bore front, while Kennedy et al. (2016) computed swash zone inertial forces to be a
 390 significant fraction of drag forces, particularly for larger boulders where the relative importance
 391 of inertia is known to increase (Dean and Dalrymple, 1991). Dimensional Froude scaling
 392 suggests that, in a bore, $\frac{DU}{Dt} = C_g g$ (irrespective of scale!), with constant of proportionality C_g
 393 that will likely vary strongly with the detailed setting. In this case, maximum inertial forces may
 394 be written as

$$395 \quad F_I = \rho_w C_m Vol \frac{DU}{Dt} = \rho_w C_m Vol C_g g = \rho_w g C_{1(-)} Vol \quad (4)$$

396 where $C_{1(-)}$ is a composite factor including inertial coefficients and acceleration. For drag forces,
 397 some significant simplifications may be established if we make a few assumptions about flow in
 398 the bore. If the boulder size at initiation of motion is roughly proportional to flow depth in the
 399 bore as would be expected from basic scaling, i.e. $(a, b, c) \propto (h + \eta)$, then boulder drag forces
 400 may be written as

$$401 \quad F_d = 0.5 \rho_w C_d a c C_f (g (h + \eta)) Fr = \rho_w g C_{2(-)} Vol \quad (5)$$

402 where $C_{2(-)} = 0.5 C_d Fr \frac{Vol}{C_f a c (h + \eta)}$ is another composite factor that will depend on boulder
 403 shape among other factors. (We note that this assumption will not hold for strongly mobile
 404 boulders, whose dimensions will not scale with water depth.) Thus, it appears likely that both
 405 drag (4) and inertial (5) forces will have the same basic form for incipient motion in overland
 406 bores. Because of this, it is reasonable for relations such as (1-2) to combine drag and
 407 acceleration into one form: here for simplicity we will eliminate inertia and increase the mean
 408 value of drag coefficient to $C_d = 1.5$ from drag-only value of $C_d = 1.05$; however, there is very
 409 little guidance on how to do this. Finally, we note the assumption that bore depth at the boulder
 410 location, $h + \eta$, is proportional to boulder size also has strong implications in that, all other

411 things being equal, a boulder with doubled size will require double the inundation depth or local
412 wave height.

413

414 3.3 Coefficient Variation and Application to Haiyan

415 Although many studies have defined and used similar hydrodynamic and friction coefficients,
416 there is still substantial uncertainty about their values: since boulders are irregular, wall-bounded
417 and not free-stream, exist in finite water depths, and may be in environments with nearby flow
418 obstructions, standard laboratory values (e.g. Dean and Dalrymple, 1991) may not apply. Here,
419 we address this by treating all values as probabilistic and compute a Monte Carlo simulation of
420 the fluid velocities required for initiation of motion for boulders measured here. Random
421 realizations of parameters were generated as follows:

$$\begin{aligned} \varepsilon &= 0.28(0.6 + 0.8R_\varepsilon) \\ \mu_s &= 0.75(0.7 + 0.6R_u) \\ C_d &= 1.5(0.7 + 0.6R_d) \\ C_l &= 0.178(0.7 + 0.6R_d) \\ \rho_s &= 2500(0.95 + 0.1R_\rho) \text{ kg/m}^3 \end{aligned} \tag{6}$$

423 where all $R_{(-)}$ are independent random variables with uniform probability distribution over the
424 range [0,1]. All dimensionless coefficient ranges are plausible based on judgement, while mean
425 densities of 2500kg/m^3 were measured from nine small samples of the native limestone.

426

427 As shown in Table 1, it was generally clear for the largest boulders measured here whether they
428 had been overturned during transport, moved through sliding only, or arose from joint-bounded
429 dislocation and transport. Thus, random simulations of parameters were used to estimate
430 incipient motion velocities for individual boulders using equations (1-3) as appropriate. Figure
431 15 shows means and standard deviations of velocities and masses for Monte Carlo simulations
432 with 10^4 random realizations for each boulder. Masses and velocities for rectangular prisms as
433 given by Nandasena et al. (2011) are also shown for comparison, using hydrodynamic
434 coefficients taken at the means of the ranges in (6).

435

436 Initial observations from Fig. 15 show that mean masses of the shaped boulders are strongly
437 reduced from rectangular prism values, as would be expected. Mean stochastic masses for
438 parameters employed here are 0.64 times those for rectangular prisms: other assumptions for the
439 probability distribution of ε would of course provide different values. (We note that Engel and
440 May (2012) and May et al. (2015) assumed masses were 0.6 times those for rectangular prisms
441 as the result of detailed boulder measurements.) Additional detailed measurements of boulder
442 shapes (Gienko et al., 2014), concentrating on parameters $(C_v, C_f, C_p, \varepsilon)$ and moment arms
443 would clearly prove helpful to better define these values, but the ranges used here seem
444 reasonable for now.

445

446 In addition to smaller masses, non-rectangular boulder shapes and probabilistic coefficients infer
447 smaller incipient motion mean velocities for all transport modes. Sliding velocities differed
448 slightly (~13% decrease), with lower submerged masses partially offset by lower frontal surface
449 areas. Joint-bounded/lifting incipient velocities also decreased noticeably (~12%), although
450 values for joint-bounded transport remain much higher than for other modes. The greatest
451 decrease in computed incipient velocities arises in overturning transport. Here, largely due to the
452 reduction of the gravitational moment arm, overturning velocities were by ~35% from
453 rectangular prism values, which is a very large difference. Without these corrections, overturning
454 velocities significantly exceeded those for sliding velocities, enough so that the differences in
455 inferred velocities were somewhat problematic for boulders in the same areas. However,
456 corrections for non-prismatic shape decrease overturning velocities enough that they are similar
457 to sliding velocities. If the mean drag coefficient were decreased from 1.5 to 1.05 (as was
458 assumed if drag and inertial forces were not combined), incipient velocities increase by ~15%
459 (results not shown), so the uncertainty in inertial terms also adds significant uncertainty to
460 inferred velocities.

461

462 Effects of uncertainties are significant: considering the largest moving blocks, ranges of
463 inundation velocities for sliding and overturning are around 5-9m/s, with coefficient uncertainty

464 driving much of this range, and variations between individual boulders also important. All of
465 these values are reasonable for a storm such as Haiyan (Roeber and Bricker, 2015), and give an
466 estimate of the range of possible conditions on top of these low cliffs. However, the range is
467 large enough that the direct inference of wave heights would be problematic.

468

469 Stationary blocks, represented here with the velocities predicted to cause incipient sliding, have
470 plausible ranges of 6-9m/s, which possibly represents a (weak) division between moving and
471 stationary boulders. However, there is significant overlap so the division is not perfect. Still, the
472 presence of large stationary blocks does help to establish upper limits on velocities.

473

474 Relations to initiate joint-bounded transport using probabilistic relations with non-prismatic
475 boulders give mean fluid velocities of 18-22m/s for the two instances observed here, while
476 prismatic values are 22-23 m/s. All of these are much higher than inferred for other transport
477 modes. (We also note that an estimate of incipient transport velocity for joint-bounded boulder
478 ESA 5 in May et al. [2015] also greatly exceeds incipient velocity estimates for boulders with
479 other transport modes.) These inferred velocities for joint-bounded transport are not credible, and
480 yield local significant wave heights of around 40m using Nott's [2003] widely-used assumption
481 of a local Froude number of unity for storm waves, $H = U^2 / g$ with non-prismatic shapes and
482 stochastic coefficients. However, Nott's companion assumption that tsunamis have Froude
483 numbers of two gives inferred tsunami heights of 10m, which are more plausible for a coastline
484 directly facing the Philippine Trench subduction zone. Thus, without the direct confirmation of
485 transport during Haiyan, and with no coherent storm boulder ridges, standard methodology
486 would have incorrectly inferred a large, previously unknown, tsunami from observed motion of
487 these joint-bounded boulders.

488

489 Present results show clearly that simple joint-bounded transport theories do not work well here
490 for boulders on the immediate cliff edge. Velocities on the cliff face may be dominated by
491 vertical velocities with extremely high accelerations (Peregrine, 2003), and horizontal velocities
492 at the cliff edge have no real theories to fall back on. Cracks underneath the boulder, which must

493 exist to some degree prior to boulder transport, are another matter. High pressures on the cliff
494 face will propagate into these cracks, giving additional forces that do not arise from traditional
495 lift relations. Neither shallow water equations, which are often used to describe tsunami
496 evolution (Imamura et al., 2008), nor Boussinesq-type systems, which are often used to model
497 storm wave runup (Roeber and Bricker, 2015), will accurately simulate hydrodynamics for
498 vertical or near-vertical cliffs. Here, computational fluid dynamics (CFD) models or laboratory
499 experiments appear to be necessary to increase understanding in this very complex region. Until
500 then, however, results such as are found in Fig. 14 suggest that use of any incipient motion
501 relations at cliff edges to estimate incident wave heights is fraught with error, and should be
502 performed with very great caution.

503

504 **5. Conclusions**

505 Based on observations and analysis of boulder transport along a cliffed coastline during Super
506 Typhoon Haiyan, we conclude that:

- 507 • Typhoon Haiyan storm waves generated and transported isolated boulders, fields of
508 large boulders, and boulder/debris clusters (usually smaller boulders),
 - 509 ○ Some large boulders observed here had originally been generated by one or
510 more earlier inundation events and transported further landward during
511 Haiyan,
- 512 • Runup along this cliffed coastline exceeded 15.2m above MSL during Typhoon
513 Haiyan, and extended at least 280m inland in some locations,
- 514 • Volumes and masses of many boulders moved by Haiyan strongly exceed the
515 literature-reported storm wave limits of 20m³ and 20 tonnes, with measured values
516 here to 83m³ and 209 tonnes,
 - 517 ○ From present observations, and in conjunction with May et al. [2015],
518 Typhoon Haiyan has the largest clasts verified to have been transported by a
519 known storm,
- 520 • Boulder shapes that are not rectangular prisms tend to be transported more easily than
521 rectangular cross-sections, particularly for overturning motion,

- 522 • Joint-bounded boulder motion at cliff faces using initiation of motion criteria gives
523 inferred velocities that are very different from other modes of motion, and should be
524 used very cautiously,
525 • Global mass-elevation plots for storm-transported boulders in regions with extreme
526 waves show a consistent upper envelope below which transport is observed and above
527 which no transport observations exist.

528

529 **6. Acknowledgements**

530 This work was funded under NSF grants 1426445 and 1435007 (ABK), NSF GRFP 2013115239
531 (TT), and the Japan Society for the Promotion of Science Kakenhi grant (NM). Valerie Ambait,
532 Nile April Robino, Catherine Ogotia Cueva, and Ariel Getiano provided significant logistical
533 assistance to the field campaign. Discussions with Brian Atwater on an early draft helped to
534 improve the paper.

535

536 **7. References**

537 Benner, R., T. Browne, H. Bruckner, D. Kelletat, and A. Scheffers (2010), Boulder transport by
538 waves: progress in physical modelling, *Zeitschrift für Geomorphologie*, 54(S3), 127-146.

539 Bourgeois, J., and B. MacInnes (2010), Tsunami boulder transport and other dramatic effects of
540 the 15 November 2006 central Kuril Islands tsunami on the island of Matua, *Zeitschrift für*
541 *Geomorphologie*, 54(S3), 175-195.

542 Cox, R., Zentner, D.B., Kirchner, B.J., and M.S. Cook (2012), Boulder ridges on the Aran
543 Islands (Ireland): Recent movements caused by storm waves, not tsunamis, *J. Geol.*, 120(3),
544 249-272.

545 Dean, R.G., and Darymple, R.A. (1991), *Water Wave Mechanics for Engineers and Scientists*,
546 World Scientific, Singapore.

547 Engel, M., and S.M. May (2012), Bonaire's boulder fields revisited: evidence for Holocene
548 tsunami impact on the Leeward Antilles, *Quaternary Science Reviews*, 54, 126-141.

549 Erdmann, W., Kelletat, D., Schaffers, A.M., and Haslett, S. (2015). *Origin and Formation of*
550 *Coastal Boulder Deposits at Galway Bay and the Aran Islands, Western Ireland*. Springer,
551 Heidelberg.

552 Fichaut, B., and S. Suanez (2011), Quarrying, transport, and deposition of cliff-top deposits
553 during extreme storm events: Banneg Island, Brittany, *Marine Geology*, **283**, 36-55.

554 Ford, D., and Williams, P. (2007), *Karst hydrogeology and geomorphology*, Wiley, Chichester.

555 Frohlich, C., M.J. Hornbach, F.W. Taylor, C.-C. Shen, A. Moala, A.E. Morton, and J. Kruger
556 (2009), Huge erratic boulders in Tonga deposited by a prehistoric tsunami, *Geology*, 37(2),
557 131-134.

558 Goto, K., M. Kunimasa, T. Kawana, J. Takahashi, and F. Imamura (2011), Emplacement and
559 movement of boulders by known storm waves – Field evidence from the Okinawa Islands,
560 Japan, *Marine Geology*, 283, 66-78.

561 Hansom, J.D., N.D.P. Bartrop, and A.M. Hall (2008). Modelling the processes of cliff-top
562 erosion and deposition under extreme storm waves, *Marine Geology*, 253, 36-50.

563 Hisamatsu, A., K. Goto, and F. Imamura (2014), Local paleo-tsunami size evaluation using
564 numerical modeling for boulder transport at Ishagaki Island, Japan, *Episodes*, 37(4), 265-276.

565 Imamura, F., Goto, K., and Ohkubo, S. (2008), A numerical model for the transport of a boulder
566 by a tsunami, *Journal of Geophysical Research – Oceans*, 113, C01008,
567 doi:10.1029/2007JC004170.

568 Jensen, A., Pedersen, G.K., and Wood, D.J. (2003), An experimental study of wave run-up at a
569 steep beach, *J. Fluid Mech.*, 486, 161-188.

570 Joint Typhoon Warning Center (2013), Haiyan Best Track, retrieved from
571 http://www.usno.navy.mil/NOOC/nmfc-ph/RSS/jtwc/best_tracks/2013/2013s-
572 [bwp/bwp312013.dat](http://www.usno.navy.mil/NOOC/nmfc-ph/RSS/jtwc/best_tracks/2013/2013s-bwp/bwp312013.dat).

573 Kennedy, A.B., Mori, N., Zhang, Y., Yasuda, T., Chen, S.-E., Tajima, Y., Pecor, W., and Toride,
574 K. (2016), Observations and modeling of coastal boulder transport and loading during Super
575 Typhoon Haiyan, *Coastal Engineering Journal*, doi:10.1142/S0578563416400040.

576 Kelletat, D., Scheffers, A., and Scheffers, S. (2004), Holocene tsunami deposits on the
577 Bahaman Islands of Long Island and Eleuthera, *Zeitschrift für Geomorphologie*, 48(4), 519-
578 540.

579 Khan, S., E. Robinson, D.-A, Rowe, and R. Coutou (2010), Size and mass of shoreline boulders
580 moved and emplaced by recent hurricanes, Jamaica, *Zeitschrift für Geomorphologie*, 54(S3),
581 281-299.

582 Mas, E., Bricker, J., Kure, S., Adriano, B., Yi, C., Suppasri, A., and Koshimura, S. (2015), Field
583 survey report and satellite image interpretation of the 2013 Super Typhoon Haiyan in the
584 Philippines, *Natural Hazards and Earth System Sciences*, 15(4), 805-816.

585 May, S.M., Engel, M., Brill, D., Cuadra, C., Lagmay, A.M.F., Santiago, J., Suarez, J.K., Reyes,
586 M., and Brückner, H. (2015), Block and boulder transport in Eastern Samar (Philippines)
587 during Supertyphoon Haiyan, *Earth Surface Dynamics*, 3, 543-558.

588 McFadgen, B.G., and Yaldwyn, J.C. (1984), Holocen sand dunes on Enderby Island, Auckland
589 Islands, *N.Z. J. Geology and Geophysics*, 27(1), 27-33.

590 Mori, N., M. Kato, S. Kim, H. Mase, Y. Shibutani, T. Takemi, K. Tsuboki, and T. Yasuda
591 (2014), Local amplification of storm surge by Super Typhoon Haiyan in Leyte Gulf,
592 *Geophys. Res. Lett.*, 41, doi:10.1002/2014GL060689.

593 Mylroie, J.E. (2008), Late Quaternary sea-level position: evidence from Bahamian carbonate
594 deposition and dissolution cycles, *Quaternary International*, 183, 61-75.

595 Nandasena, N.A.K., R. Paris, and N. Tanaka (2011), Reassessment of hydrodynamic equations:
596 Minimum flow velocity to initiate boulder transport by high energy events (storms,
597 tsunamis), *Marine Geology*, 281, 70-84.

598 Nandasena, N.A.K., Tanaka, N., Sasaki, Y., and M. Oda (2013), Boulder transport by the 2011
599 Great East Japan tsunami: Comprehensive field observations and whether model predictions?
600 *Marine Geology*, 346, 292-309.

601 National Disaster Risk Reduction and Management Council (2014), [NDRRMC update: SitRep](#)
602 [No. 108 Effects of Typhoon “YOLANDA” \(HAIYAN\)](#), Retrieved May 29, 2015.

603 Nott, J. (2003), Waves, coastal boulder deposits and the importance of the pre-transport setting,
604 *Earth and Planetary Science Letters*, 210, 269-276.

605 Paris, R., P. Wassmer, J. Sartohadi, F. Lavigne, B. Barthomeuf, E. Desgages, D. Grancher, P.
606 Baumert, F. Vautier, D. Brunstein, and C. Gomez (2009), Tsunamis as geomorphic crises:
607 lessons from the December 26, 2004 tsunami in Lhok Nga, West Banda Aceh (Sumatra,
608 Indonesia), *Geomorphology*, 104, 59-72.

609 Paris, R., Naylor, L.A., and W.J. Stephenson (2011), Boulders as a signature of storms on rock
610 coasts, *Marine Geology*, 283, 1-11.

611 Peregrine, D.H. (2003), Water-wave impact on walls, *Ann. Rev. Fluid Mech.*, 35, 23-43.

612 Ramalho, R.S., Winckler, G., Madeira, G., Helffrich, G.R., Hipólito, A., Quartau, R., Adena, K.,
613 and J.M. Schaefer (2015). Hazard potential of volcanic flank collapses raised by new
614 megatsunami evidence, *Science Advances*, doi:10.1126/sciadv.1500456.

615 Roeber, V., and J.D. Bricker (2015), Destructive tsunami-like wave generated by surf beat over a
616 coral reef during Typhoon Haiyan, *Nature Communications*, 6, 7854,
617 doi:10.1038/ncomms8854.

618 Scheffers, A., Scheffers, S., and D. Kelletat (2005), Paleo-tsunami relics on the southern and
619 central Antillean island arc, *Journal of Coastal Research*, 21(2), 263-273.

620 Scheffers, A., and S. Kinis (2014), Stable imbrication and delicate/unstable settings in coastal
621 boulder deposits: indicators for tsunami dislocation? *Quaternary International*, 332, 73-84.

622 Shah-hosseini, M., Morhange, C., Beni, A.N., Marriner, N., Lahijani, H., Hamzeh, M., and
623 Sabatier, F. (2011), Coastal boulders as evidence for high-energy waves on the Iranian coast
624 of Makran, *Marine Geology*, 290, 17-28.

625 Shimozono, T., Y. Tajima, A.B. Kennedy, H. Nobuoko, J. Sasaki, and S. Sato (2015), Combined
626 infragravity wave and sea-swell runup over fringing reefs by super typhoon Haiyan, *J.*
627 *Geophys. Res.-Oceans*, doi:10.1002/2015JC010760.

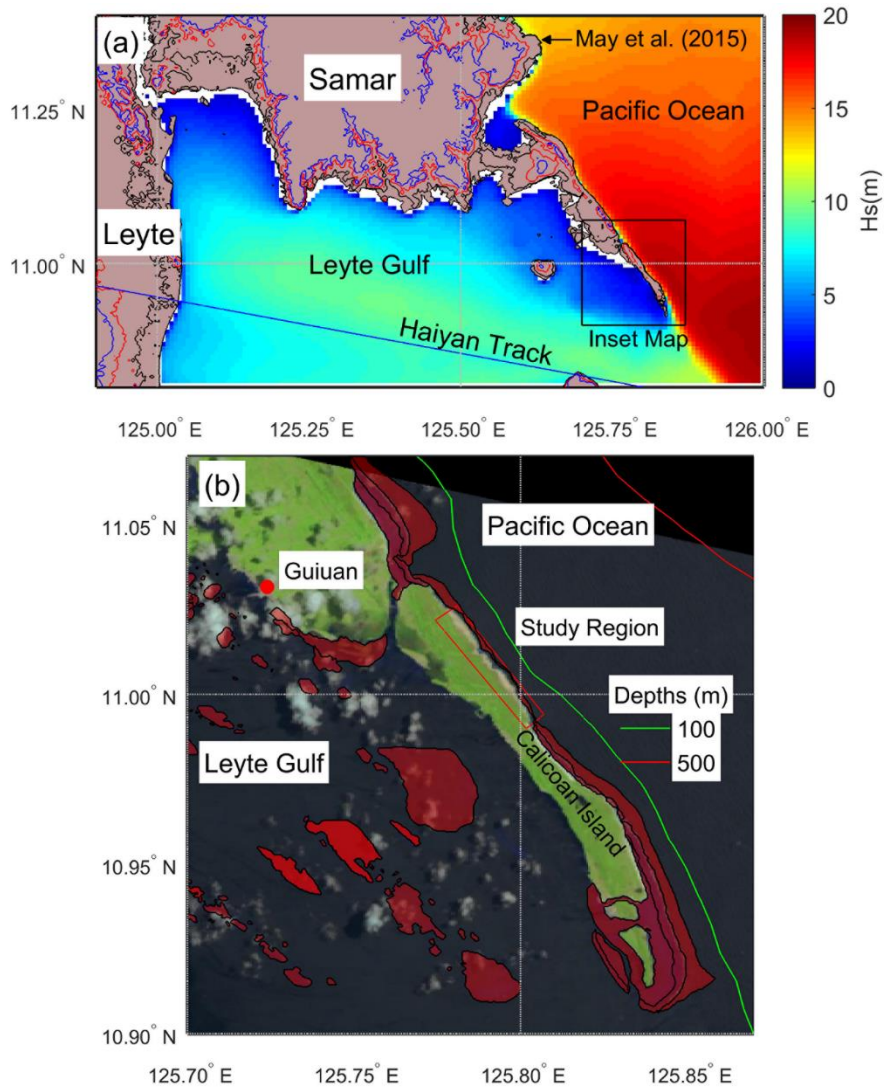
- 628 Taborosi, D., and Kazmer, M. (2013), Erosional and Depositional Textures and Structures in
629 Coastal Karst Landscapes, Coastal Research Library, Vol 5., 15-57.
- 630 Tajima, Y., T. Yasuda, B.M. Pacheco, E.C. Cruz, K. Kawasaki, H. Nobuoka, M. Miyamoto, Y.
631 Asano, Y., T. Arikawa, N. Ortigas, R. Aquino, W. Mata, J. Valdez, and F. Briones (2014),
632 Initial report of JSCE-PICE joint survey on the storm surge disaster caused by Typhoon
633 Haiyan, *Coastal Engineering Journal*, 56, 1450006.
- 634 Watt, S.E., Jaffe, B.E., Morton, R.A., Richmond, B.M., and G. Gelfenbaum (2010). *Description*
635 *of extreme-wave deposits on the northern coast of Bonaire, Netherlands, Antilles*, Open-File
636 Report 2010-1180, U.S. Geological Survey, Reston, Virginia.
- 637 Williams, D.M., and Hall, A.M. (2004), Cliff-top megaclast deposits of Ireland, a record of
638 extreme waves in the North Atlantic – storms or tsunamis? *Marine Geology*, 206, 101-117.
- 639

640 Table 1. Characteristics of measured boulders with a-axis greater than 5m. Boulders marked by * could not be reached with RTK
 641 GPS, and their elevations are estimates only.

ID	Latitude	Longitude	a (m)	b (m)	c (m)	Ground Elev (m)	Top Elev (m)	x (m)	Δx (m)	Vol (m ³)	Mass (t)	Observed Motion
South Region												
B53-3	10.999316	125.798082	5.2	3.6	1.85	11.6	13.3	108		20.8	52	Overturning
999	11.000487	125.798321	7.3	5.1	3.2	11.1	14.3	30	30	71.5	179	Joint Bounded
B3	11.001121	125.797323	7.2	5.0	2.7	9.9	13.0	124		58.3	146	Overturning
B108	11.005203	125.794453	6.9	3.3	2.55	8.8	11.9	109		34.8	87	Overturning
A003	11.005234	125.794300	6.2	3.6	2.68	7.5	10.3	97		35.9	90	Sliding
S1	11.004425	125.795566	7.4	3.26	2.3	7.9	11.1	59		33.3	82	Sliding
1122-A	11.004196	125.795224	5.1	2.5	2.3		12.8	104		17.6	44	Overturning
B70	11.002839	125.796205	6.1	5.4	2.8	11.3	13.5	102		55.3	138	Sliding
B71	11.002965	125.796038	5.9	3.7	2.9	11.5	14.2	106		38.0	95	Overturning
North Region												
N0	11.014232	125.786753	5.9	3.1	2.8		15.2	65	12	30.7	77	Sliding
N1	11.012470	125.786755	6.1	3.0	2.6	7.8	10.1	65	45-60	28.6	71	Sliding
N2	11.010163	125.789890	7.45	4.9	3.1	7.3	10.4	27	21	67.9	170	Joint Bounded
B343*	11.023268	125.780017	7.7	5.5	2.3	5-9		92		58.4	146	Overturning
B358*	11.023597	125.780120	5.95	3.5	2.0	5-9		56		25.0	62	Sliding
B345*	11.022797	125.780442	7.7	5.3	3.4	5-9		105		83.3	208	Sliding
B320	11.020260	125.782330	7.3	5.6	3.4	7.00	9.7	130		83.4	208	Sliding
B321	11.020365	125.782259	7.4	4.5	2.8	6.4	8.7	127		55.9	140	Sliding
B342a	11.021368	125.780824	5.3	2.9	1.8	7.6	9.5	168		16.6	41	Sliding
B327	11.021267	125.781356	6.3	4.4	2.4	6.5	9.1	132		39.9	100	Overturning
B327b	11.021278	125.781199	6.0	3.9	3.4	6.6	9.4	144		47.7	119	Overturning
No Motion												
B122	11.003293	125.796156	7.5	6.5	4.5	9.2	11.5	82	0	131.6	329	No Motion
B311	11.019267	125.783896	8.0	5.0	2.7		12.6	69	0	64.8	162	No Motion

642

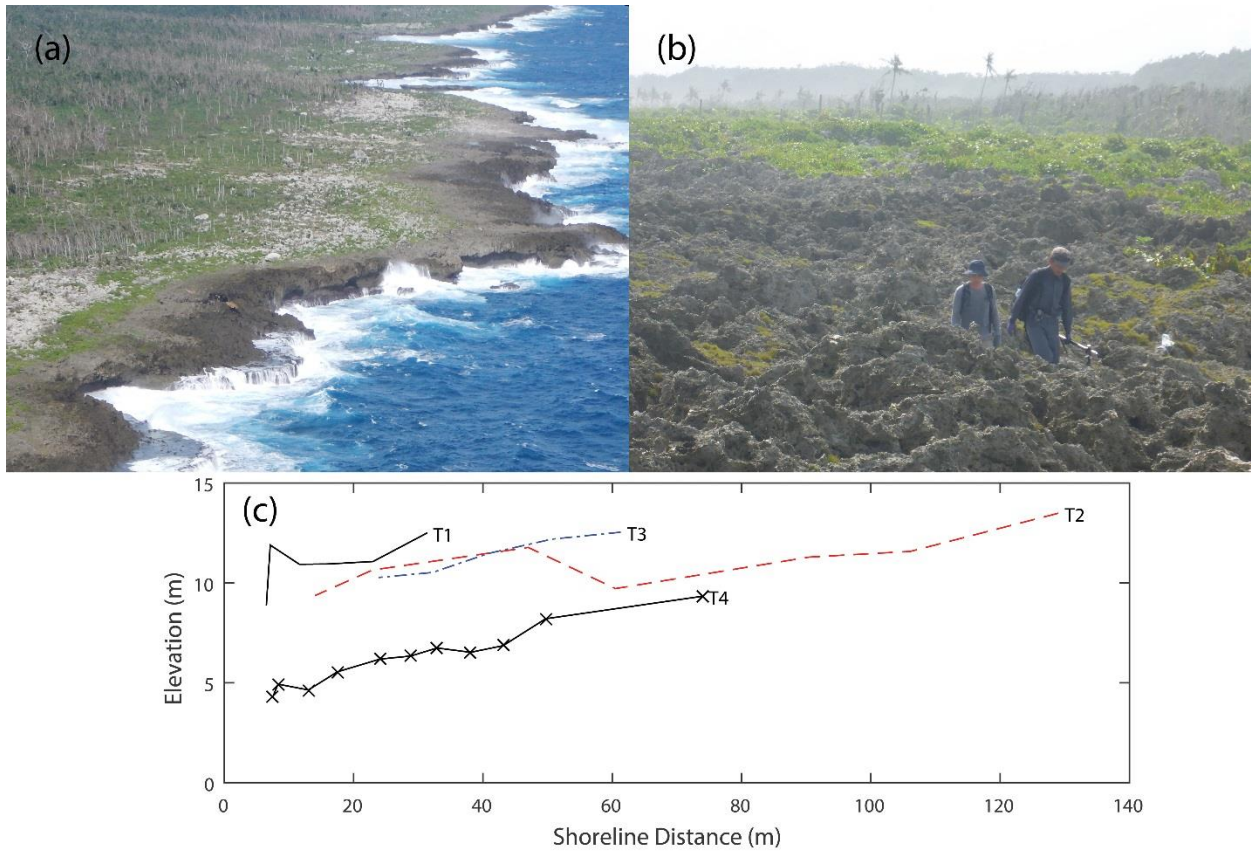
643 **Figures**



644

645 Figure 1. Typhoon Haiyan and study region on Calicoan Island. (a) Overview map showing
646 Haiyan Track, (10,50,100) meter elevation contours, and hindcast wave heights; (b) Inset map of
647 study region on Calicoan Island, depth contours, and coral reef locations in red. Background
648 image from Landsat May 2, 2014.

649



650
 651 Figure 2. (a) Aerial view of a portion of the study region, facing northwest; (b) Rough phytokarst
 652 topography in the sea-spray region; (c) Partial elevation transects. Locations are shown in Figure
 653 5.

654

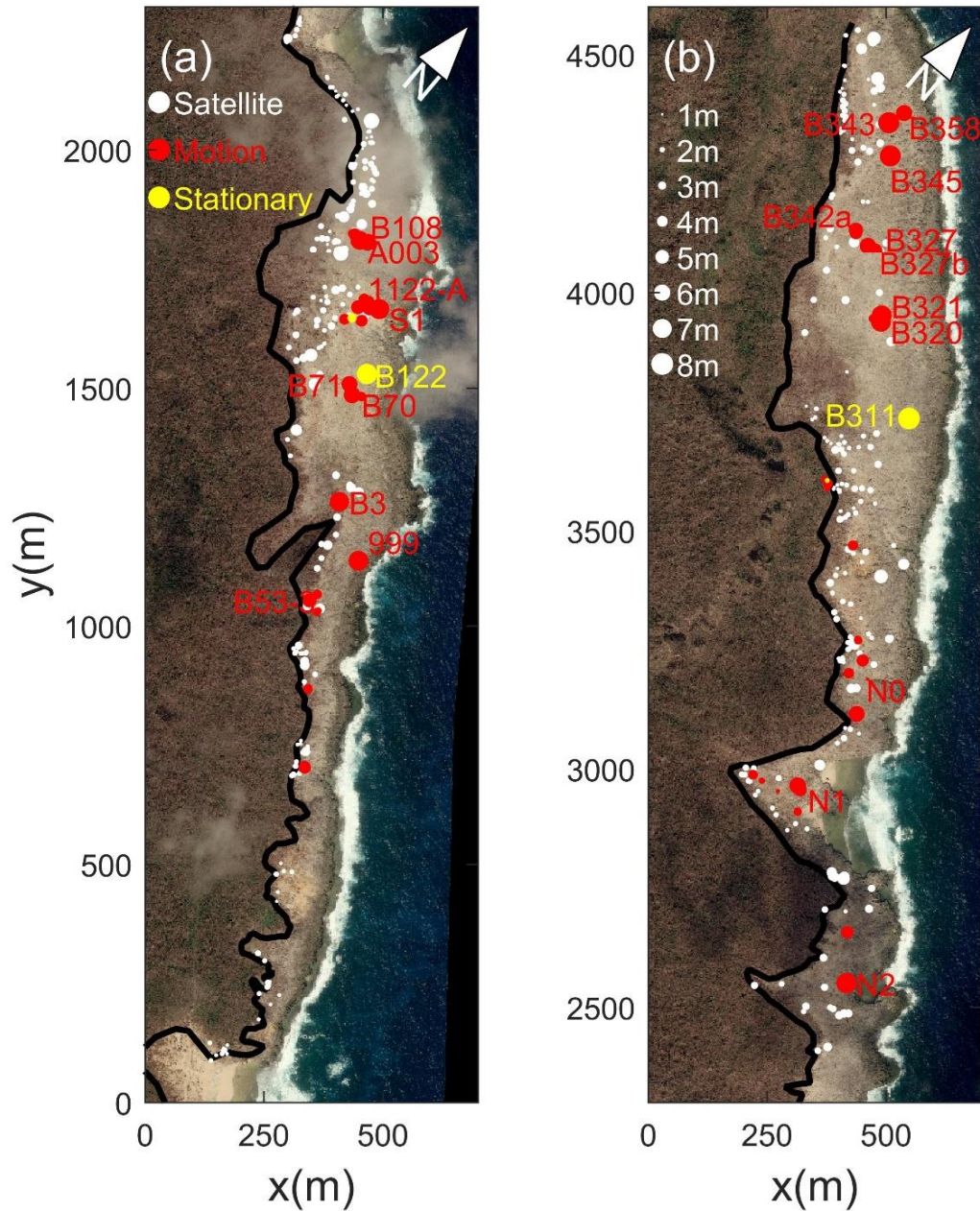


655

656 Figure 3. Example of low elevation blocks and boulders in pocket beach that were not measured.
657 Location is shown in Fig. 5.

658

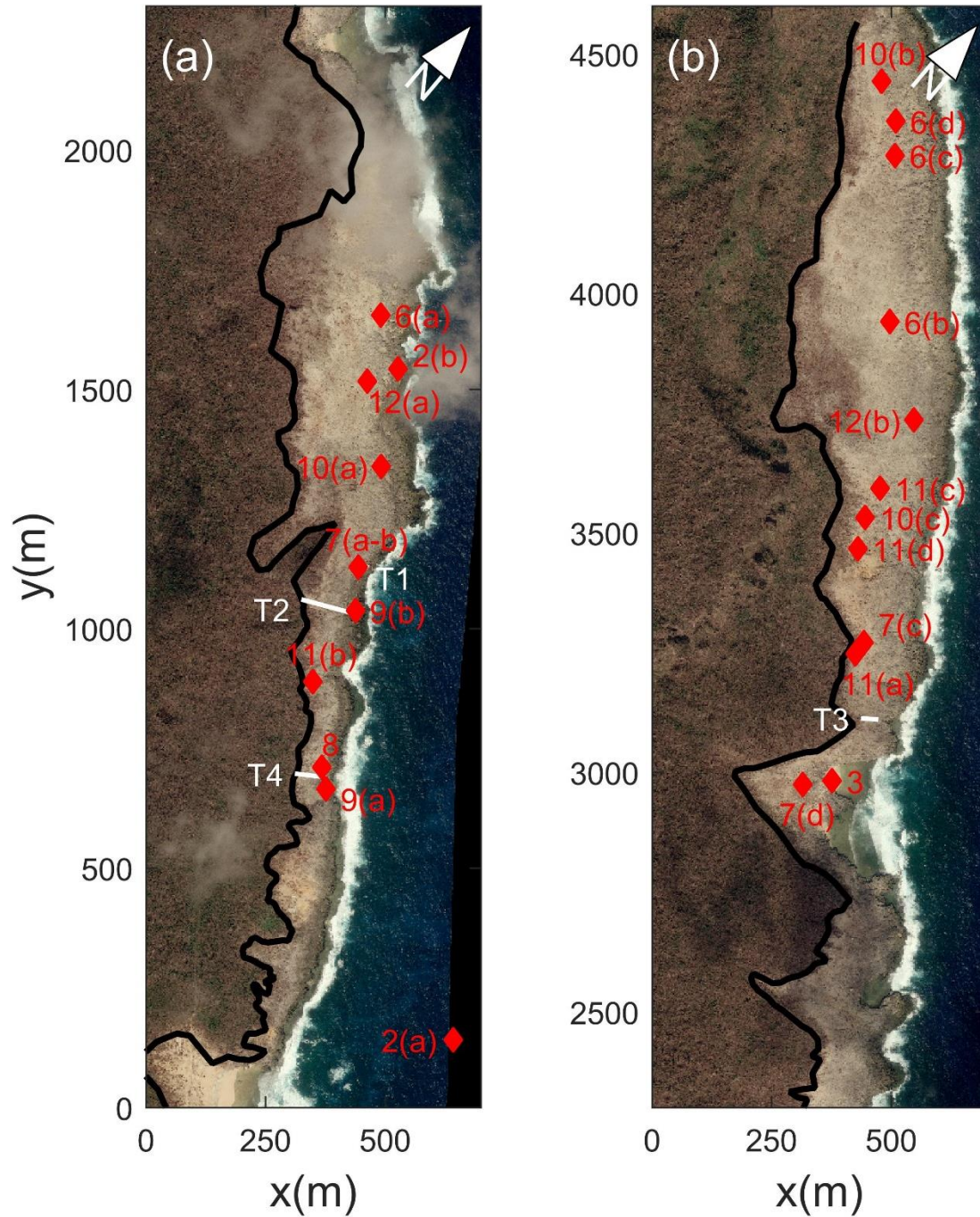
659



660

661 Figure 4. Runup inland extent (black line), boulder locations (●) (white symbols: satellite
 662 observations; red: ground observations of transported boulders; yellow: ground observations of
 663 stationary boulders); length of a-axis. (a) $y=0-2300\text{m}$ alongshore coordinate (south region of
 664 study area); (b) $y=2300-4600\text{m}$ (north region). Background image taken December 15, 2013
 665 from Pleiades 1B satellite.

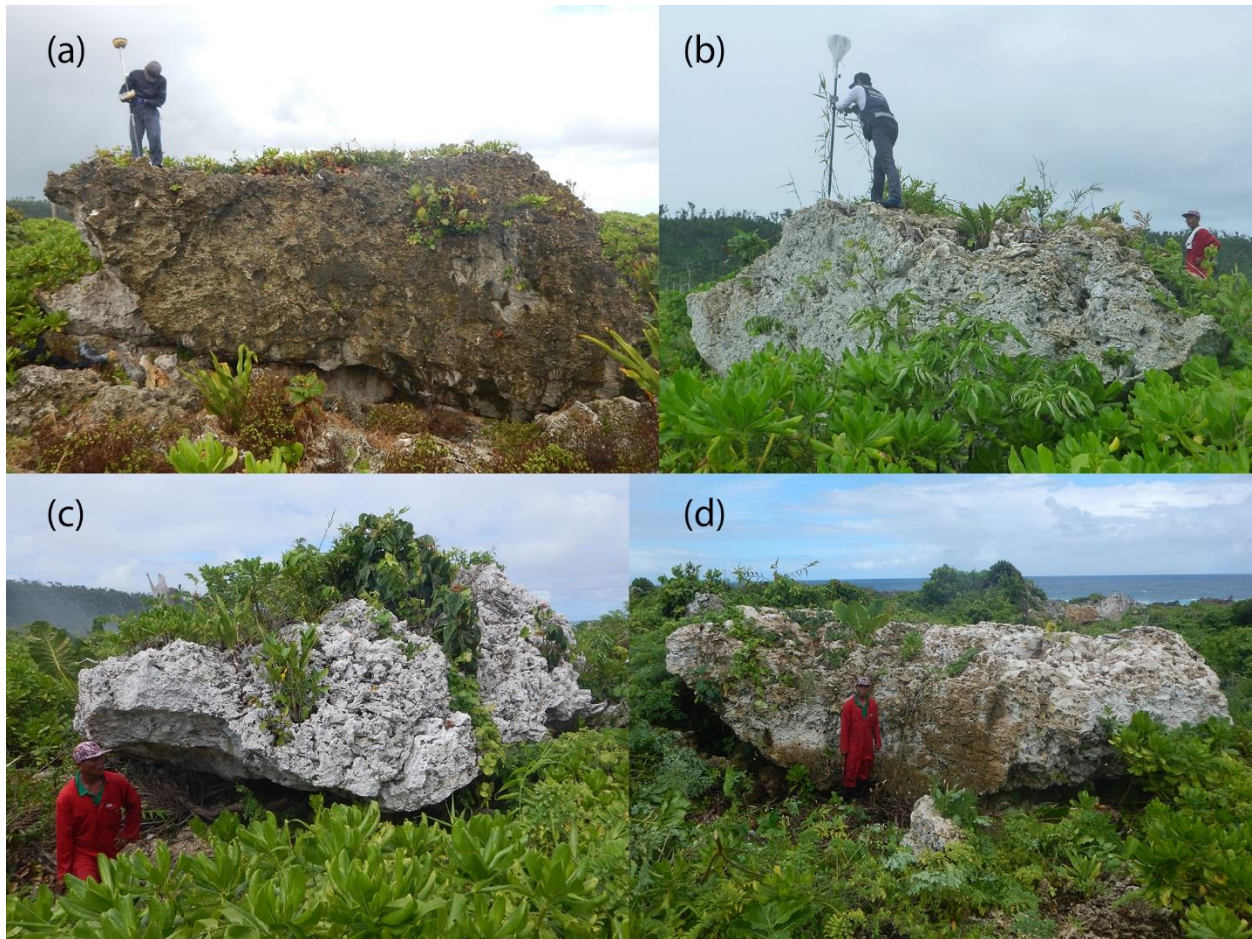
666



667

668 Figure 5. Locations of Figures referenced in this paper. (a) $y=0-2300\text{m}$ alongshore coordinate
 669 (south region of study area); (b) $y=2300-4600\text{m}$ (north region). Background image taken
 670 December 15, 2013 from Pleiades 1B satellite.

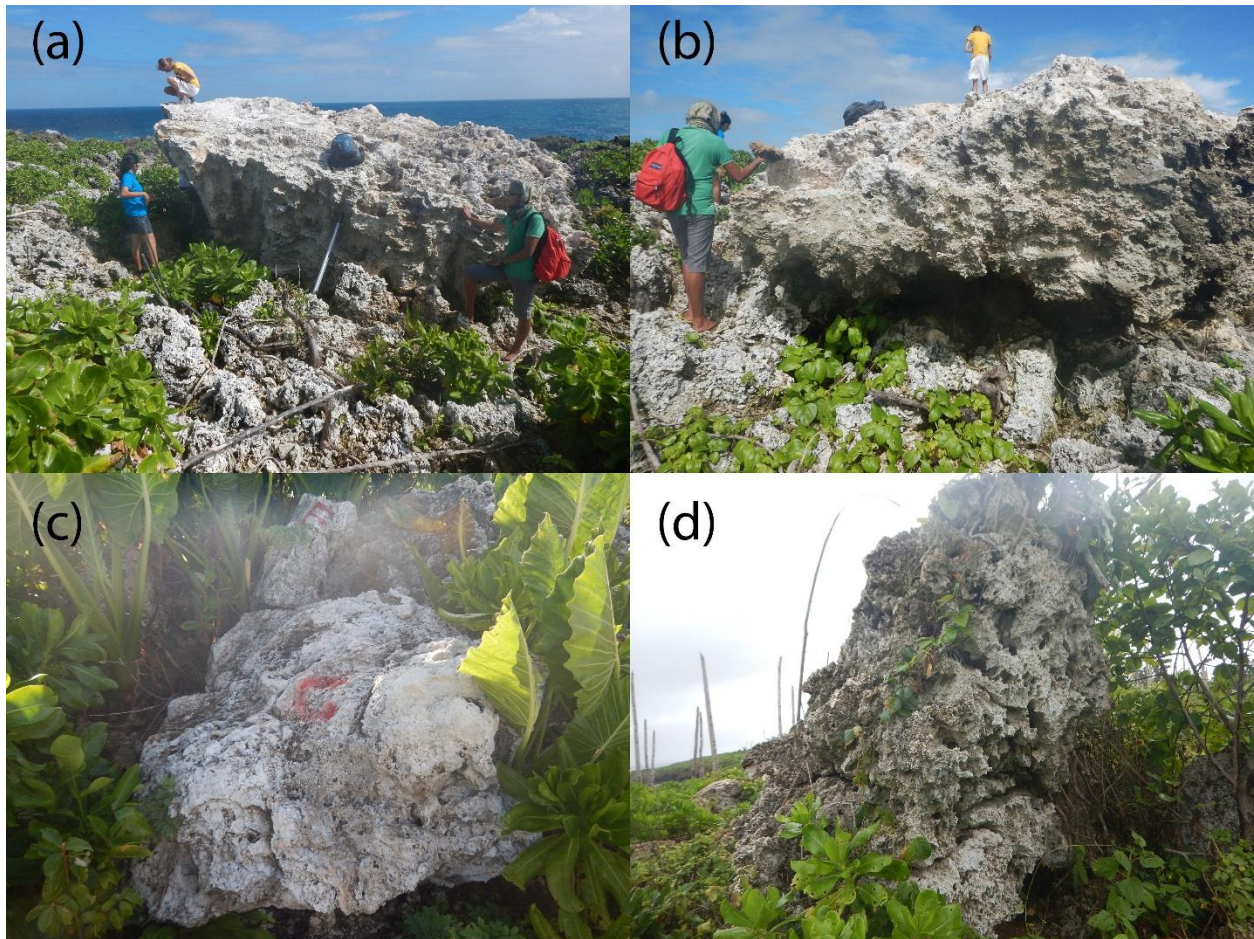
671



673
674 Figure 6. Examples of large boulders transported by Typhoon Haiyan waves. (a) S1; (b) B320;
675 (c) B345; (d) B343. Additional photos and settings for all large boulders are given in
676 Supplemental Figures S.1.1-S.1.15. Locations are shown in Figures 4-5.

677

678



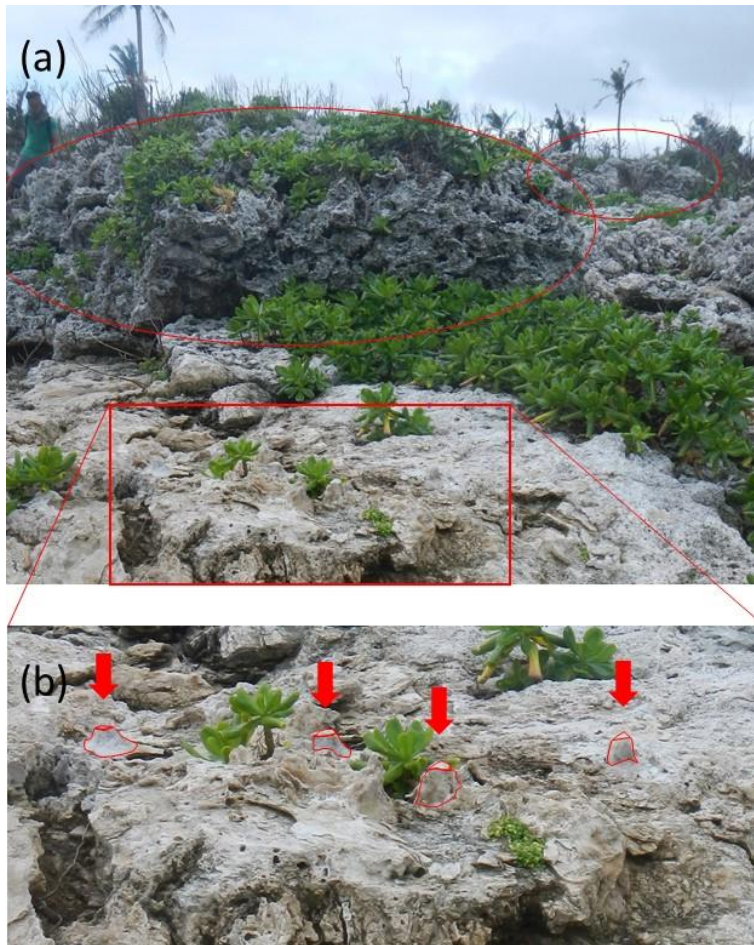
679

680 Figure 7. Weathering and angularity differences across observed boulders. (a-b) Front and back
681 sides of Boulder 999, showing more exposed (rough gray), and protected (smoother white) pre-
682 storm surfaces; (c) pre-storm underside of overturned boulder showing smooth, white
683 depositional karst features; (d) Very angular transported boulder whose dark gray left side was
684 directly exposed to sea spray pre-storm. Locations are shown in Fig. 5.

685

686

687

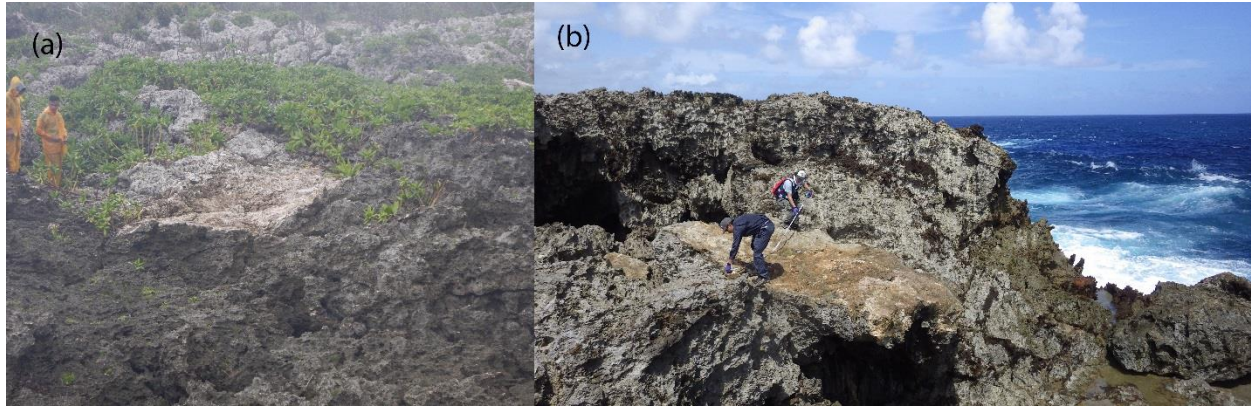


688

689 Figure 8. Karst features generated underneath boulders that were transported during Haiyan. (a)
690 Transported boulders (circled), and overall setting; (b) Inset of bedrock with arrows showing
691 karst solution columns that were attached to boulder undersides pre-storm. Location is shown in
692 Fig. 5.

693

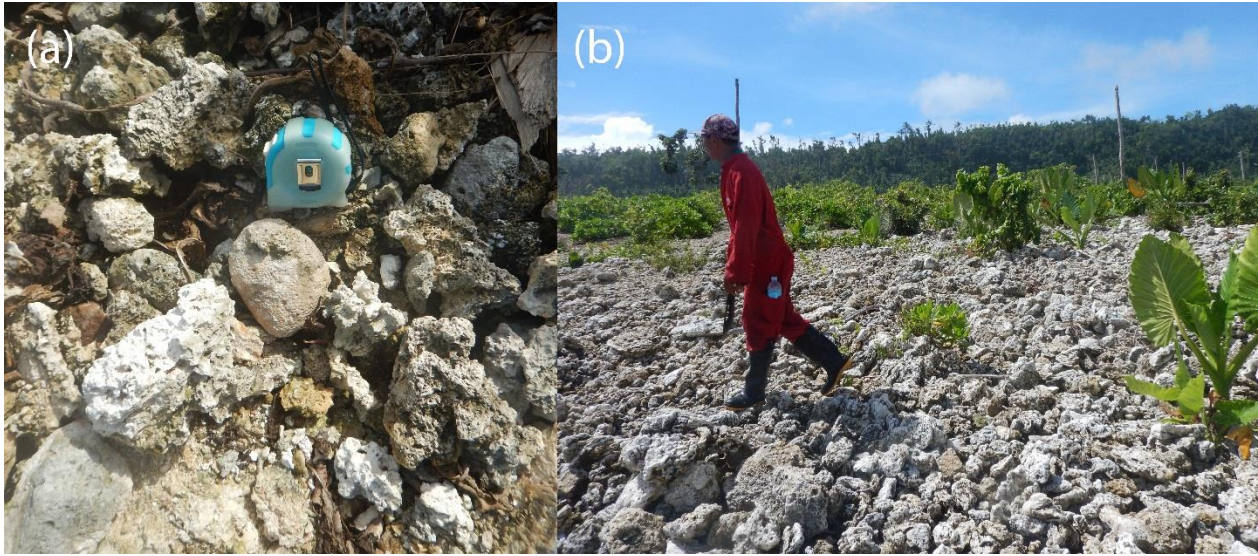
694



695

696 Figure 9. Typical whitish to brownish clifftop scars from rock breakage and transport during
697 Haiyan. Locations are shown in Figure 5.

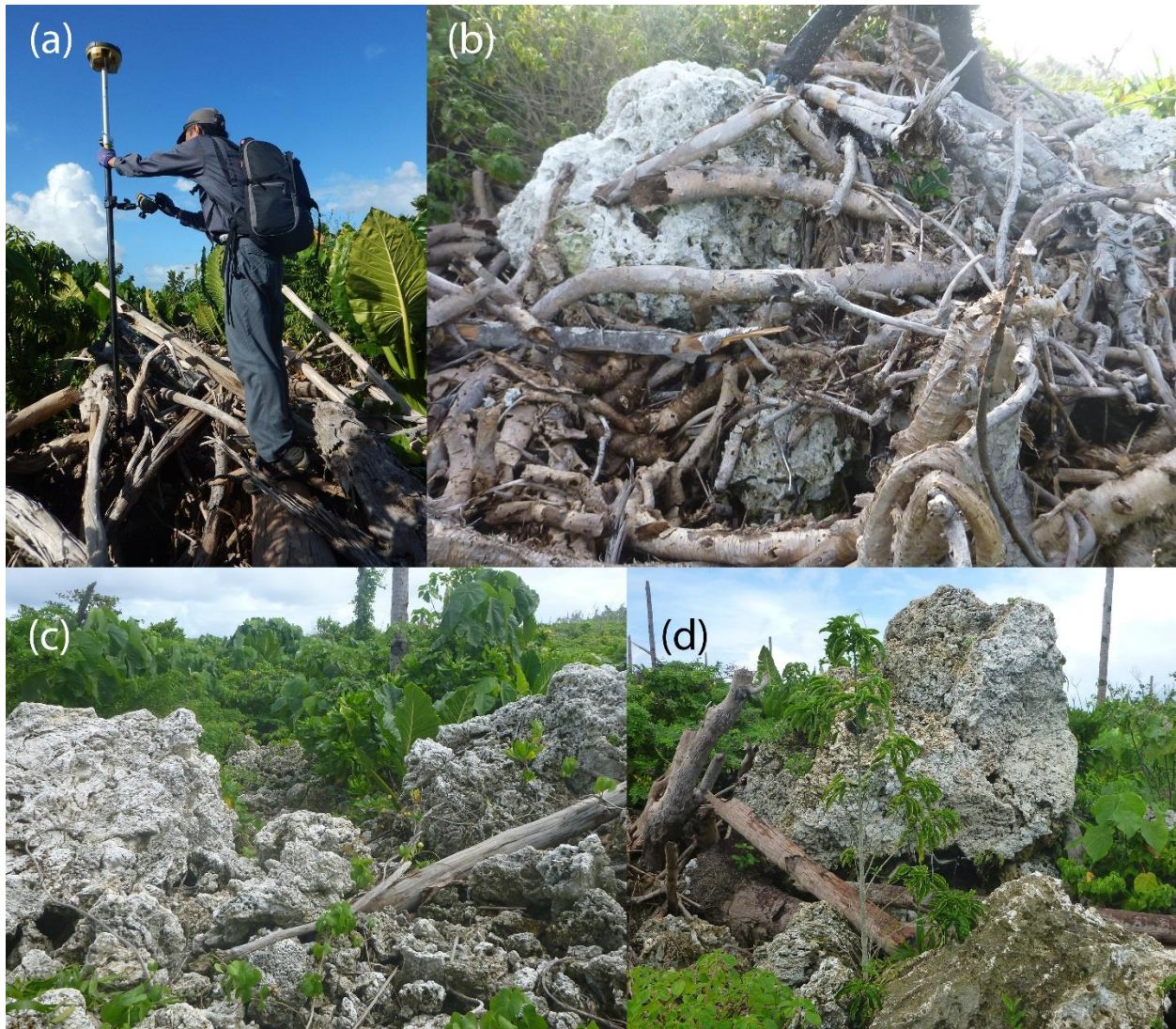
698



699

700 Figure 10. Inland beaches from Haiyan runup. (a) Cobble beach, showing relatively rare clast of
701 subaqueous origin (rounded) surrounded by very angular to angular subaerially-generated clasts;
702 (b) Boulder/cobble beach approximately 100 m inland. Locations are shown in Figure 5.

703

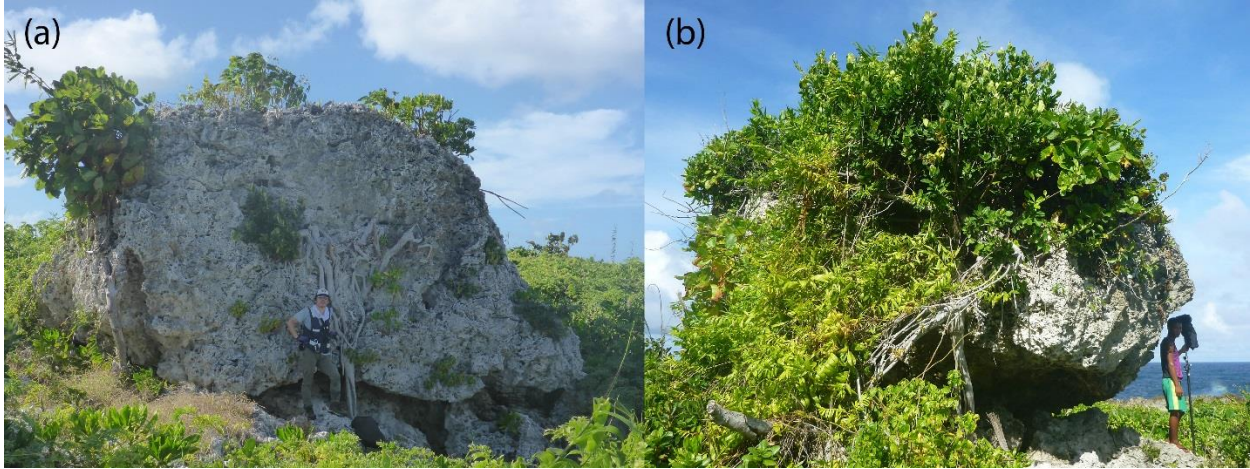


705

706 Figure 11. Debris clusters generated by Haiyan runup. (a) Vegetative debris (mostly trees and
 707 woody shrubs); (b) Mixed boulder/vegetative debris; (c-d) Mostly rocky debris clusters.

708 Locations are shown in Figure 5.

709

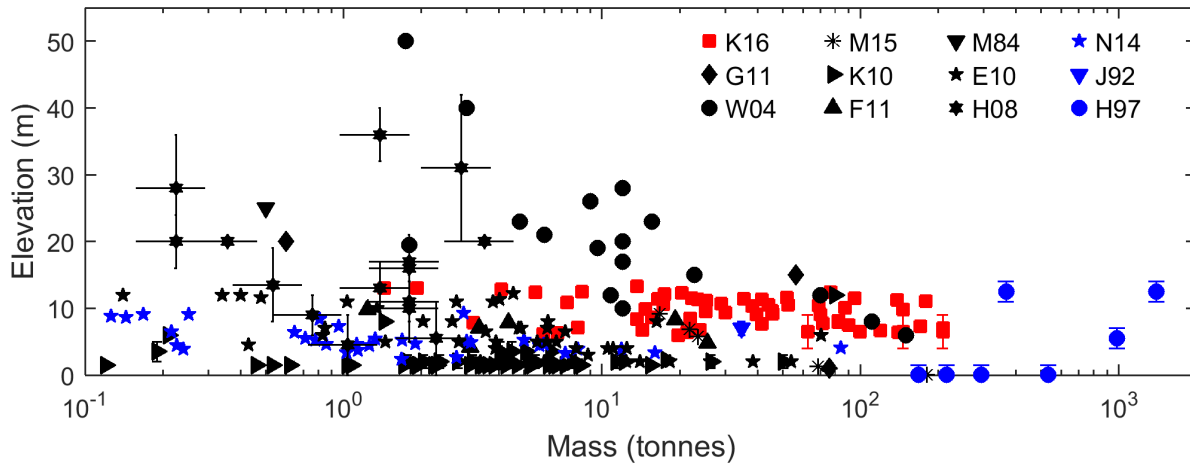


710
711 Figure 12. Large blocks that did not move during Haiyan. (a) B122; (b) B311. Locations are
712 shown in Figs. 4-5, and aerial photographs are in supplemental Figs S.2.1-S.2.2.

713

714

715

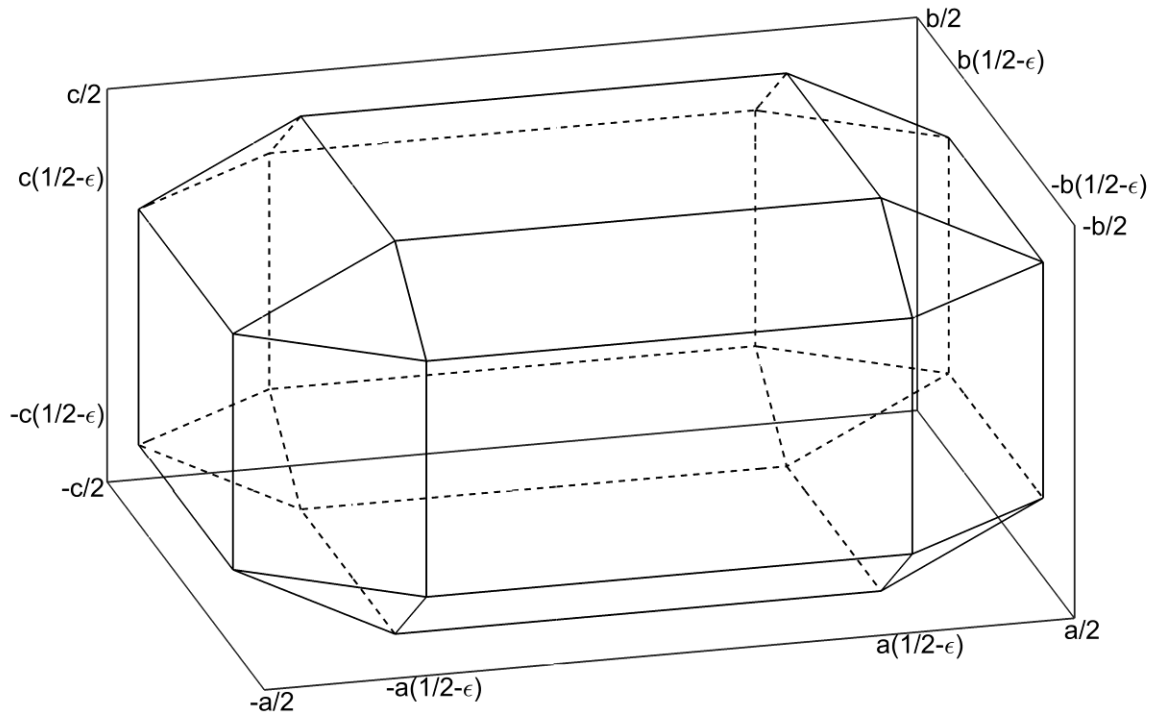


716

717 Figure 13. Masses of coastal boulders transported by known storm waves as a function of
718 ground elevation: (■) Present study; (◆) Okinawan Islands, Goto et al. (2011); (●) Aran Islands,
719 Ireland, Williams and Hall (2004); (*) Typhoon Haiyan, May et al. (2015); (▶) Jamaica, Khan
720 et al. (2010); (▲) Banneg Island, France, Fichaut and Suanez (2011); (▼) Enderby Island,
721 McFadgen and Yalwyn (1984); (pentagram) Iceland, Etienne and Paris (2010); (hexagram+error
722 bars) Scotland, Hansom et al. (2008). Boulders with indeterminate or disputed origins:
723 (pentagram) Lanyu Island, Taiwan, Nakamura et al. (2014); (▼) Grand Cayman Island, Jones
724 and Hunter (1992); (●) Eleuthera Island, Bahamas, Hearty (1997).

725

726



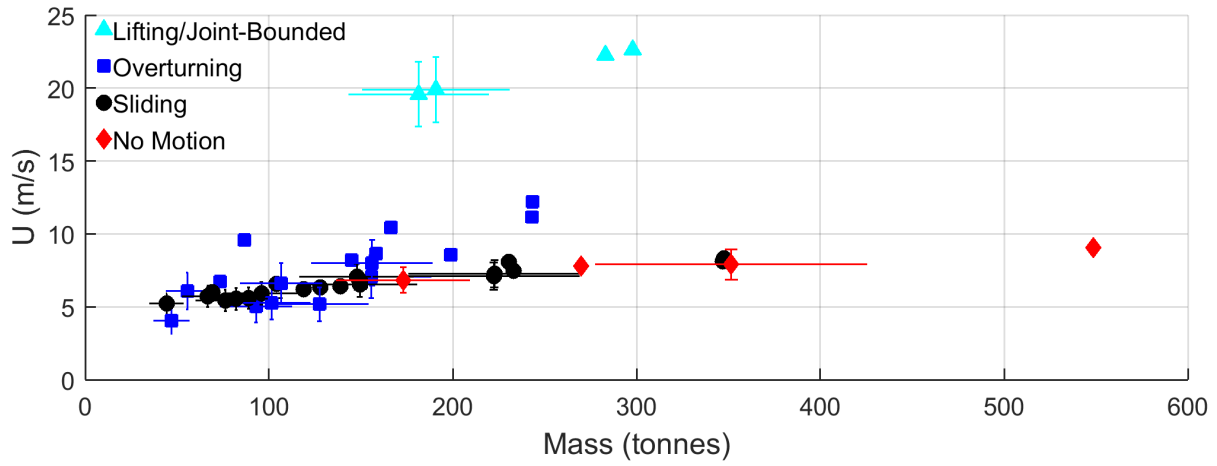
727

728 Figure 14. Definition sketch for reduced boulders, with hidden edges shown as dashed lines.

729

730

731



732

733 Figure 15. Probabilistic inferred initiation of motion fluid velocities for large boulders measured
734 here using Equations (1-3,6), showing 1-sigma error bars. Symbols without error bars show
735 deterministic relations of Nandasena et al. (2011) for rectangular prisms.

736

737